Surface oxide-rich activation layer (SOAL) on Ni_2Mo_3N for rapid and durable oxygen evolution reaction

Yao Yuan,[1,2,8] Samira Adimi,[1,8] Xuyun Guo,[3,8] Tiju Thomas,[4] G. Sudha Priyanga,[4] Haichuan Guo,[1] Pilsun Yoo,[5] Jiacheng Wang,[6] Ye Zhu,[3] Peilin Liao,[5]* J. Paul Attfield,[7]* Minghui Yang[1,2]*

[1] Ningbo Institute of Materials Technology and Engineering, Chinese Academy of Sciences, 1219 Zhongguan West Road, Ningbo 315201, China.

[2] Center of Materials Science and Optoelectronics Engineering, University of Chinese Academy of Sciences, Beijing 100049, China.

[3] Department of Applied Physics, The Hong Kong Polytechnic University, Hung Hom, Kowloon, Hong Kong, China.

[4] Department of Metallurgical and Materials Engineering, Indian Institute of Technology Madras Adyar, Chennai 600036, Tamil Nadu, India.

[5] School of Materials Engineering, Purdue University, West Lafayette, IN 47907, United States.

[6] State key Laboratory of High Performance Ceramics and Superfine Microstructure, Shanghai Institute of Ceramics, Chinese Academy of Sciences, 1295 Dingxi Road, Shanghai 200050, China.

[7] Centre for Science at Extreme Conditions and School of Chemistry, University of Edinburgh, King's Buildings, Mayfield Road, Edinburgh, EH9 3JZ, UK.

[8] These authors contributed equally to this work.

Corresponding Authors

*E-mails: myang@nimte.ac.cn; j.p.attfield@ed.ac.uk; lpl@purdue.edu

Abstract

The oxygen evolution reaction (OER) is key to renewable energy technologies such as water electrolysis and metal-air batteries. However, the multiple steps associated with proton-coupled electron transfer result in sluggish OER kinetics and catalysts are required. Here we demonstrate that a novel nitride, Ni_2Mo_3N, is a highly active OER catalyst that outperforms the benchmark material RuO_2. Ni_2Mo_3N exhibits a current density of 10 mA cm^{-2} at a nominal overpotential of 270 mV in 0.1 M KOH with outstanding catalytic cyclability and durability. Structural characterization and computational studies reveal that the excellent activity stems from formation of a

surface oxide-rich activation layer (SOAL). Secondary Mo atoms on the surface act as electron pumps that stabilize oxygen-containing species and facilitate the continuity of the reactions. This discovery will stimulate further development of ternary nitrides with oxide surface layers as efficient OER catalysts for electrochemical energy devices.

Developing new chemistry for renewable energy technologies has become a key requirement to satisfy rising global energy demand. The oxygen evolution reaction (OER) is one of the essential half-reactions for many renewable energy applications.[1] Despite being thermodynamically favorable, the OER suffers from the sluggish kinetics.[2, 3] Ru- and Ir-based materials are the benchmark catalysts for OER.[4, 5], but their high costs and scarcity diminish the technological prospects for the OER. An ideal OER catalyst must be highly efficient, stable, and active at a potential minimally above the thermodynamic value (1.23 V *vs.* RHE). However, up to now, no materials have reached this threshold.

Recently, metal nitrides have been found to possess good electrocatalytic activity toward OER, such as Fe_xN,[6] Co_4N,[7] Ni_3N,[8] HfN,[9] and Ni_3FeN,[10] which have stimulated considerable research on exploiting efficient metal nitrides catalysts. In these cases, however, the nitride-based catalysts are still insufficiently efficient and the activity mechanism is still obscure. Both experimental and theoretical results indicate that earth abundant first-row (3d) transition metal (especially Ni-based) materials can accelerate the adsorption of oxygen-containing intermediates.[11-13] This is shown to be promising for overcoming usual kinetic barriers associated with

OER.[14, 15] Hence, Ni-based materials have been extensively studied as electrocatalysts towards OER, such as NiTe/NiS,[16] CoNi hydroxide,[17] $NiFeO_xH_y$,[18] and $IrNiO_x$.[19]. In this work, a urea-glass route is employed to synthesize a ternary nitride Ni_2Mo_3N which is found to be an outstanding OER catalyst. The excellent OER activity observed stems not only from the unique electronic nature of bimetallic nitrides, but also from the surface oxide-rich activation layer (SOAL) with active Ni-sites and the Mo electron pumps, which is formed spontaneously during electrocatalytic oxidation process.

Results and Discussion

Crystalline powders of Ni_2Mo_3N were prepared via the urea-glass route (see Methods for details). A polymer-like gel was prepared by mixing nickel chloride, molybdenum chloride and urea in ethanol, for form a precursor for direct nitridation. Urea acts as the nitrogen source and bonds with metal through coordinate covalent bonds (C=O→M) in the gel (Supplementary Fig. 1 and Table S1).[20] These bonds dissociated to yield reductive species for nitridation at a rather modest temperature.[21, 22]

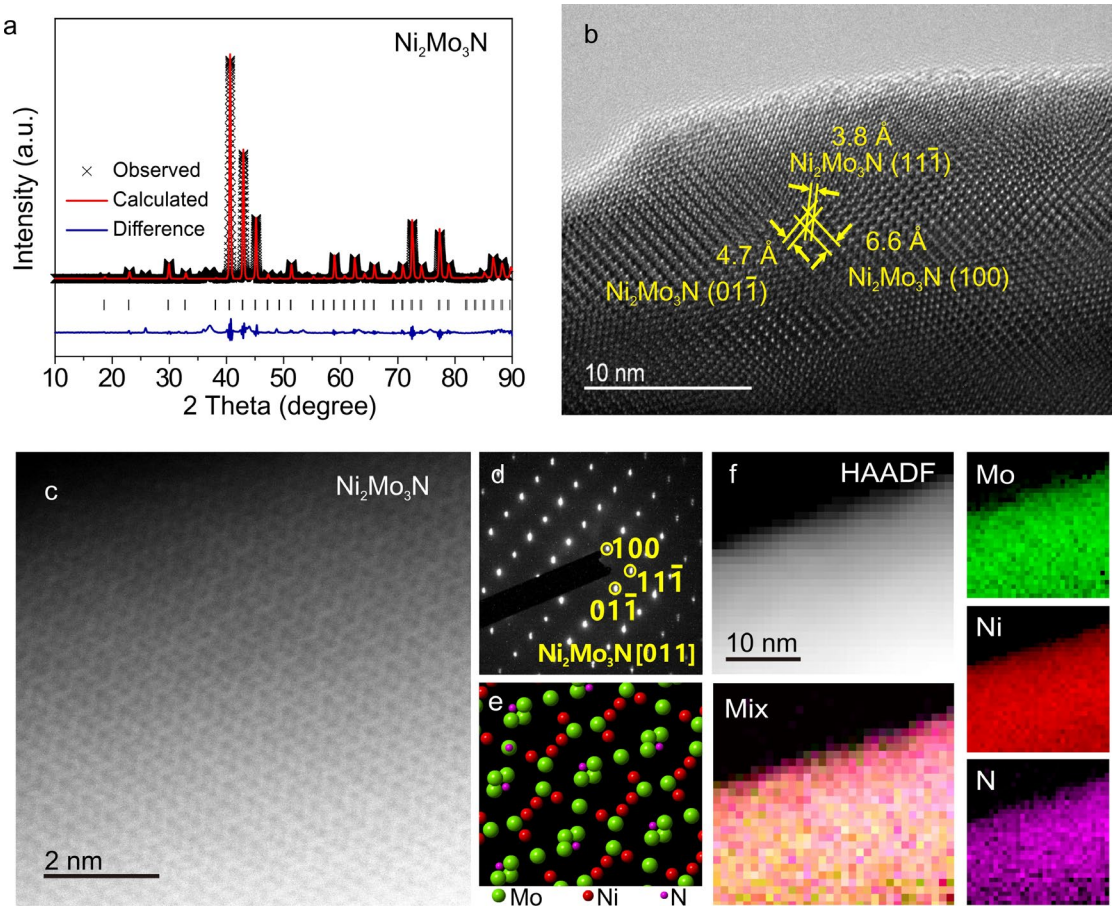

Fig. 1 | Characterization of as-prepared Ni_2Mo_3N. (a) Rietveld fitted XRD pattern of Ni_2Mo_3N. (b) HRTEM image of Ni_2Mo_3N reveals well-resolved lattice fringes, which are in agreement with the (100), (01$\bar{1}$) and (11$\bar{1}$) planes of cubic Ni_2Mo_3N with no distinct surface phases. (c) HAADF-STEM image, (d) SAED pattern and (e) Ni_2Mo_3N atomic structure. (f) HAADF-STEM image and corresponding EELS elemental mapping of Ni, Mo and N elements of Ni_2Mo_3N.

Crystalline Ni_2Mo_3N formed is confirmed using X-ray powder diffraction (XRD) pattern in Fig. 1a. The obtained diffraction peaks for Ni_2Mo_3N correspond to the cubic *β*-Mn structure (space group: *P*4-32) with unit cell parameter *a*=11.0270(2) Å (Supplementary Fig. 1c); a trace amount of impurity can be found, as indicated by a tiny and broad reflection peak at ~37.5°. The particle size is ~44 nm, as calculated by Scherrer's formula. There is no evidence of formation of any surface phase according to the transmission electron microscopy (TEM) results (Fig. 1b-f). As shown by the high resolution TEM (HRTEM) image in Fig. 1b, the Ni_2Mo_3N lattice fringes with 4.7

Å for $(01\bar{1})$, 6.6 Å for (100) and 3.8 Å for $(11\bar{1})$ planes are detected, in which $(01\bar{1})$ is perpendicular to (100) plane. The corresponding selected area electron diffraction (SAED) pattern can be indexed to the cubic Ni_2Mo_3N single crystal with the zone axis [011]. Furthermore, the high-angle annular dark field scanning TEM (HAADF-STEM) image and the corresponding electron energy-loss spectroscopy (EELS) elemental maps in Fig. 1f offers evidence of a uniform distribution of Ni, Mo and N elements in the as prepared ternary nitride.

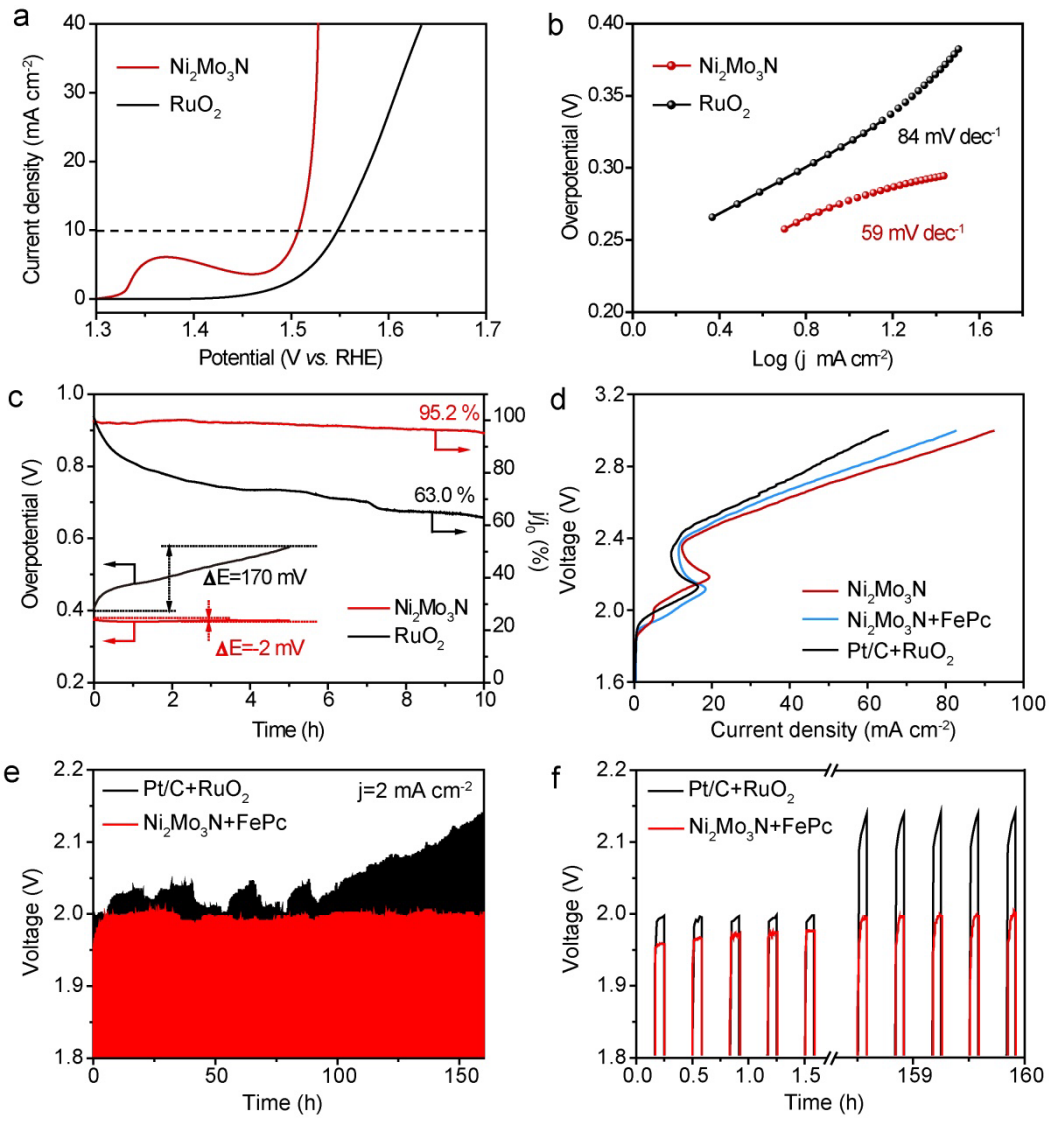

Fig. 2 | OER catalysis properties of samples in 0.1 M KOH solution and corresponding Zn-air battery performances. (a) OER polarization curves of Ni_2Mo_3N and commercial RuO_2 at a scan rate of 5 mV s^{-1} and (b) the corresponding Tafel plots. The Tafel plots are fitted to the

equation: $\eta = b \log j + a$, where η is the overpotential, j is the current density, and b is the Tafel slope. (c) Chronoamperometric and chronopotentiometric responses of Ni_2Mo_3N and RuO_2 for OER. (d) Charge polarization curves of Zn-batteries for Ni_2Mo_3N, Ni_2Mo_3N+FePc and Pt/C+RuO_2 as the air electrode catalysts. (e, f) Charge/discharge cycling of a rechargeable Zn-air battery based on Ni_2Mo_3N +FePc and Pt/C+RuO_2 at 2 mA cm^{-2}.

To evaluate the OER electrocatalytic activity of ternary nitride Ni_2Mo_3N, electrochemical experiments were performed in an alkaline solution. For comparison, RuO_2 (one of the best known OER catalysts), Ni_3N, and Mo_2N were also examined (Supplementary Fig. 3). The OER catalytic performances are investigated using linear sweep voltammetry (LSV) in 0.1 M O_2-saturated KOH solution (Fig. 2a and Supplementary Fig. 4). Compared to binary nitride samples, Ni_2Mo_3N exhibits superior current density and the most negative OER onset potential (Supplementary Fig. 5a). For Ni_2Mo_3N, a current density of 10 mA cm^{-2} can be achieved at a nominal overpotential of 270 mV, while Ni_3N and Mo_2N need a relatively large overpotential of 360 and 450 mV, respectively. This result clearly suggests that Ni_2Mo_3N has significant catalytic activity as the performance exceeds that of RuO_2 (320 mV). In order to gain further insight into the kinetics of the process, the corresponding Tafel plots of the catalysts are obtained from the polarization curves (Fig. 2b and Supplementary Fig. 5b). The catalyst with a lower Tafel slope favors accelerating the OER process with improved kinetics. Ni_2Mo_3N shows the smallest Tafel slope value (59 mV dec^{-1}) compared to Ni_3N (91 mV dec^{-1}) and Mo_2N (107 mV dec^{-1}). The Tafel slope of Ni_2Mo_3N is even lower than that of RuO_2 (84 mV dec^{-1}), indicating more favorable OER kinetics in case of the ternary nitride. The above results demonstrate that ternary nitride Ni_2Mo_3N with excellent OER activity superior or comparable to that of most nitride-based catalysts (Supplementary Fig. 6).

Ni_2Mo_3N offers a high electrochemical double layer capacitance (C_{dl}), which is proportional to the active surface area (Supplementary Fig. 7). The C_{dl} of Ni_2Mo_3N is found to be 3.27 mF cm^{-2}, which is ~3.8 and 1.4 times C_{dl} than that observed in case of Ni_3N (0.87 mF cm^{-2}) and Mo_2N (2.34 mF cm^{-2}), respectively (Supplementary Fig. 8). It demonstrates that the ternary nitride prepared is more effective than the binary nitride due to the higher effective surface area and a higher density of active surface sites. This correlates with Ni_2Mo_3N delivering a much higher current density than Ni_3N and Mo_2N.

The long-term stability of electrocatalysts is another key performance indicator. The chronoamperometric response reveals that Ni_2Mo_3N can maintain good catalytic activity for at least 10 h in alkaline solution, showing only a slight anodic current attenuation to 95.2 %. On the other hand, RuO_2 displays a current attenuation to 63.0 % after 10 h reaction (Fig. 2c and Supplementary Fig. 9). Chronopotentiometry is further used to evaluate the electrocatalytic durability of Ni_2Mo_3N for OER in 0.1 M KOH without *iR* compensation. The overpotential of Ni_2Mo_3N remains almost unchanged at a current density of 10 mA cm^{-2} for 5 h, whereas the overpotential of RuO_2 increases to 170 mV within 5 h (Fig. 2c). As a result, Ni_2Mo_3N demonstrates substantially enhanced stability and durability, indicating promise for prolonged OER operation.

To assess the performance of Ni_2Mo_3N in practical energy devices, it has been tested in a Zn-air battery. A rechargeable Zn-air battery was constructed using Ni_2Mo_3N and Iron phthalocyanine (FePc) (a highly active catalyst for oxygen reduction reaction) as the cathode catalyst (Supplementary Figs. 10 and 11). For comparison, another battery

was fabricated using a precious-metal Pt/C and RuO_2 based composite catalyst. Fig. 2d displays the charge polarization curves of the electrodes, implying a charge performance of Ni_2Mo_3N that is better than that of RuO_2 as confirmed by its higher current densities at the same potential. In addition, the charge-discharge cycling tests were carried out at a current density of 2 mA cm^{-2}. As shown in Fig. 2e and 2f, Ni_2Mo_3N and FePc exhibits a long cycle life as evidenced by 160 h; this too is much better than the cycle life of the mixed Pt/C and RuO_2 battery. More importantly, the charging voltage of Ni_2Mo_3N is always lower than that of RuO_2, which remains stable at about 2 V. It signifies potential application of Ni_2Mo_3N in the rechargeable Zn-air battery.

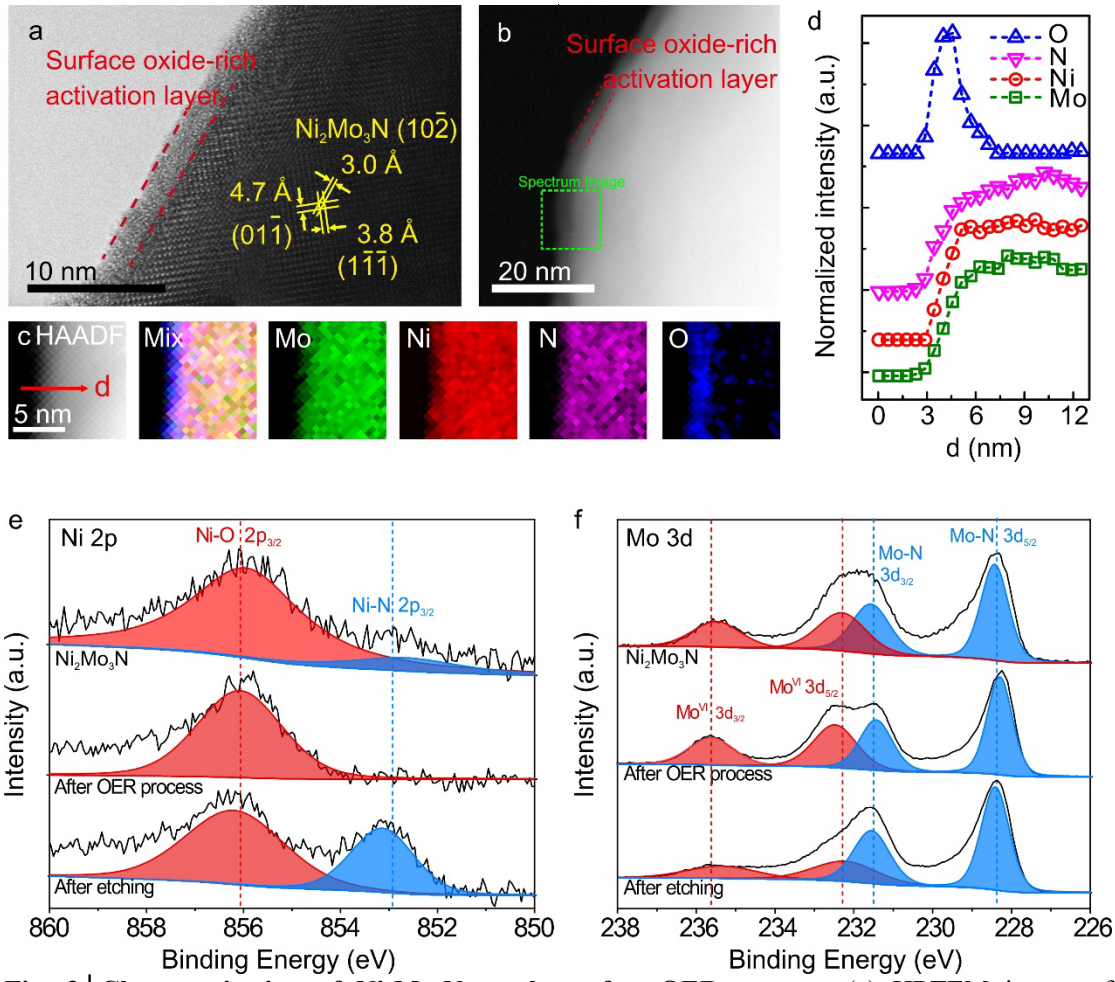

Fig. 3 | Characterisation of Ni_2Mo_3N catalyst after OER process. (a) HRTEM image of Ni_2Mo_3N after OER process. (b, c) HAADF-STEM images with EELS mapping of O, Ni and Mo

elements of Ni_2Mo_3N after OER process. (d) Corresponding EELS line-scan profiles of the surface oxide-rich activation layer. XPS spectra of Ni_2Mo_3N and used Ni_2Mo_3N before and after in-situ etching treatment in the (e) Ni 2p and (f) Mo 3d regions.

TEM is carried out to understand the surface structure after OER stability testing (Fig. 3 and Supplementary Fig. 12). As shown in Fig. 3a, the inner part of Ni_2Mo_3N is still high-crystallinity cubic structure with $(10\bar{2})$, $(1\bar{1}\bar{1})$ and $(01\bar{1})$ lattice planes resolved, which is also confirmed by the SAED pattern (Supplementary Fig. 12a inset). While at the surface, an thin surface layer ~ 2.5 nm is detected by both HR-TEM (Fig. 3a) and HAADF-STEM (Fig. 3b) after OER process, which appears to be amorphous. EELS mapping further indicates that this layer is oxygen rich (Figs. 3c,d), with less Mo compared to the inner region. Ni_2Mo_3N is an intermediate nitride having the β-Mn structure; the phase formation relies on strict stoichiometric values. Each interstitial N atom occupies the 4b site and is surrounded by six Mo atoms. This defines a corner-shared $[NMo_6]$ octahedron with short Mo-N bond distances.[23-26] It is illustrated that nitrogen atoms are closer to Mo and further away from Ni. Hence, Ni ions interact readily with exterior ligands (O^{2-}, OH^-, etc.). Catalytically active Ni ions are expected to accumulate at the surface of Ni_2Mo_3N, and become oxidized at the high potential applied during the OER process. Thus, compared with the sample before durability evaluation, an extra amorphous surface oxide-rich activation layer (SOAL) is generated on the surface of Ni_2Mo_3N. This SOAL does not just stabilize the nitride surface, but may also provide the catalytic activation site of the OER.

The SOAL is further confirmed by using X-ray photoelectron spectroscopy (XPS) (Supplementary Figs. 13 and 14). The corresponding high-resolution of Ni 2p survey for samples are shown in Fig. 3e. For Ni_2Mo_3N, the peaks of Ni-N species disappear

after OER testing along with the evolution of Ni-O, and appear again after 30 s of in-situ etching treatment. It indicates that near surface, Ni-N species are oxidized into high valence state during OER process, and the generated oxide rich layer is rather thin. The high-resolution XPS survey for Mo 3d is also displayed in Fig. 3f. Both Ni-N and Mo-N peaks shift to lower binding energies when compared with binary nitrides (Ni_3N and Mo_2N) (Supplementary Fig. 14). The negative shifts occur in the Ni 2p (Ni-N) species and Mo 3d (Mo-N) species of Ni_2Mo_3N, suggesting that the electronic structure of Ni and Mo atoms have been modified in the ternary nitride.[27] These negative shifts relate to a down-shift in the d-band center and a much higher electron density in the material, which is expected to correlate with a higher efficiency of the catalyst. After OER testing, the peaks for Mo-N remain, although the intensity becomes weaker and it is recovered again after etching treatment. This indicates that in the case of the ternary nitride, only surface Ni is significantly oxidized, while Mo is still binding with N. This is consistent with our 'SOAL' hypothesis. The electronic states of SOAL (Ni species) can be tuned based on the composition of the subsurface of the ternary nitride. This in fact is expected to offer the appropriate electronic structure for enhancement of the OER activity.

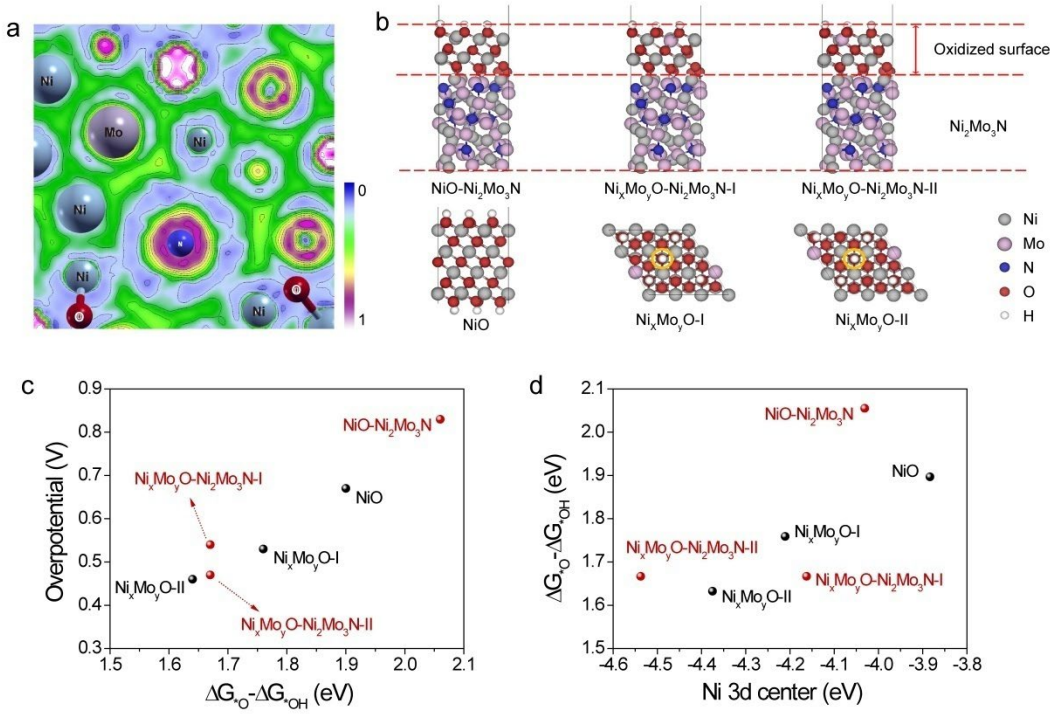

Fig. 4 | Unveiling the SOAL as the active site for an enhanced OER (a) Electron Localization Function (ELF) distribution of the (111)-Ni_2Mo_3N oxidized surface. (b) Geometry of bulk structures and slab geometry used in calculations. Ni, Mo, N, O, and H are colored as grey, purple, blue,red, and white sphere, respectively. (c) Overpotential versus reaction free energies of reaction for different systems. (d) Reaction free energy of reaction for OH deprotonation with respect to the center of occupied Ni 3d states.

It has been reported that surfaces can cause significant changes to the electronic and geometric characteristics of materials.[28, 29] The surface rearrangements make the Ni atoms the most external atoms on top of the (111)-Ni_2Mo_3N, and give more freedom to Ni atoms to be easily oxidized, forming the surface nickel oxide-rich layer (Supplementary Fig. 15). Moreover, the deduction of the Electron Localization Function (ELF) between Ni with N and Mo atoms (Supplementary Figs. 16 and 17) reveals that the bonding between them is weakened on the surface. This is in agreement with Fig. 4a for oxide surface which shows the decreased ELF and electronic charges around Mo sites on top of SOAL. These Mo atoms can be

considered as an electron pump on top of the oxide surface that transfer surface charges and facilitate the continuity of the oxygen reactions (see SI for more information).

Furthermore, previous studies of OER over Ni oxide surfaces suggest that the OER critically depends on the deprotonation of OH and formation of OOH species, with the OH deprotonation being the potential determining step.[30, 31] Fig. 4c plots the reaction potential versus reaction free energy for the deprotonation of surface OH species for different systems, with and without a SOAL (Fig. 4b, Supplementary Figs. 18 and 19, Supplementary Table S2). For SOAL without Mo, the overpotential of NiO-Ni_2Mo_3N is 0.83 V, slightly higher by 0.16 V than that of pure NiO. Mo lowers the overpotentials for both hybrid structure and pure NiO. This indicates that Mo locations near the reaction sites offer favorable energetics for the deprotonation of *OH to form *O, and facilitates the OER process.

Supplementary Table S3 also summarizes the data pertaining to the Bader charge of O atoms in the adsorbed OH species. As Mo replaces one of the Ni atoms, O anions gain extra electrons and both the Ni 3d and O 2p states are shifted to more negative energies (Supplementary Figs. 20-22). In particular, the downward shift in Ni 3d states agrees well with our XPS results. It is shown that as the Ni 3d center shifts to more negative energies, the reaction free energy of the OH deprotonation decreases and deprotonation proceeds more readily (Fig. 4d). Overall, this indicates that Mo donates extra electrons to O anions and lowers the energies of the occupied Ni 3d and O 2p states, which results in stabilization of the product *O species.

Conclusion

In summary, this report provides a simple and straightforward strategy to prepare a ternary nitride Ni_2Mo_3N showing OER electrocatalytic performance that outperforms with the standard material RuO_2 and the component binary nitrides. It offers a current density of 10 mA cm^{-2} at a nominal overpotential of 270 mV in 0.1 M KOH which is better than the state-of-the-art materials. The excellent OER performance of Ni_2Mo_3N results from the surface electronic structure of active Ni-sites and Mo electron pumps in the discovered surface oxide-rich activation layer (SOAL). This is confirmed by the experimental characterizations and theoretical calculations. This work will pave the way to synthesis and tuning of ternary nitride OER catalysts and their SOALs creating new opportunities for the development of clean energy systems.

Methods

Synthesis process

Synthesis of Ni_2Mo_3N nanoparticles

All chemical reagents were in analytical grade and used without further purification. Ni_2Mo_3N nanoparticles (NPs) were prepared using a urea-glass route. In this way, nickel chloride hydrate ($NiCl_2 \cdot 6H_2O$, 1g, ≥99%, Aladdin Industrial Corporation) and molybdenum chloride ($MoCl_5$, 1g, ≥99%, Aladdin Industrial Corporation) were dissolved in ethanol (2mL). This was done while adequately stirring to obtain a stable and brown solution. Then, urea (1g, ≥99%, Aladdin Industrial Corporation) was added to the mixed alcoholic solution. This mixture was then stirred until the urea completely dissolved to yield a clear solution. Subsequently the solution was aged for 12 h before nitridation to ensure that the metal was bonded to urea as completely as possible. The gels were then placed in a horizontal tube furnace and heated to 800°C at a ramp rate of 2 °C min^{-1} for 2h under an N_2 flow (30 ml min^{-1}). The temperature was increased slowly to avoid excessive foaming of the polymer-like cohesive and eruptive release of the leftovers of the solvent. After nitridation, the furnace was cooled down to the room temperature naturally in the same flow and passivation was done using a flow of Ar mixture (containing <0.1% O_2).

Synthesis of Ni_3N

Ni_3N was synthesized using the same procedure described above with the only difference being that no molybdenum chloride was added in this case.

Synthesis of Mo_2N

Mo_2N also was synthesized using the process described above. The only modification was that no nickel chloride hydrate was used in this case.

Characterizations

X-ray powder diffraction (XRD) was performed using a powder X-ray diffractometer (Rigaku Miniflex 600, Japan) with Cu-K_α radiation (λ = 1.54178 Å) in a 2θ range from 10° to 90° at 1°min^{-1}. Fourier Transform Infrared (FT-IR) spectra of KBr powder-pressed pellets were recorded using a Thermo NICOLET 6700. The morphology of the samples were characterized using scanning electron microscopy (SEM) (JSM-7800F, Japan). Transmission electron microscopy (TEM) and scanning TEM (STEM) were performed using JEOL JEM-2100F TEM/STEM (Japan) operated at 200 kV, equipped with INCA (Oxford, UK) energy dispersive spectroscopy (EDS) detector and Enfina (Gatan, US) energy-loss spectroscopy (EELS) detector. Spectrum imaging of EELS was carried out under 200 kV accelerating voltage with a 13 mrad convergence angle for the optimal probe condition. Energy dispersion of 0.7 eV per channel and 21 mrad collection angle were set up for EELS, High-angle annular dark-field (HAADF) images were acquired with an 89 mrad inner angle simultaneously. The Ni, Mo, and O intensity maps were extracted from the EELS spectrum image by integrating across the energy windows of 854-876(L2,3 edge), 228-242(M4,5 edge), and 532-543(K edge) eV, respectively. The intensity map for N was extracted using multiple linear least squares fitting (MLLS) in the DigitalMicrograph (Gatan, USA) software. X-ray photoelectron spectroscopy (XPS, VG ESCALAB MKII, USA) with Mg-K_α as the excitation source was used to analyze the valence of the atoms on the surface with contaminated C as internal standard (C1s=284.6 eV).

Electrochemical measurements

The OER electrochemical measurements were carried out in a three-electrode system using a rotating disk electrode (RDE) (PINE Instrument) at a rotation speed of 1600rpm with an electrochemical workstation (CHI660E, CH Instrument). A glassy carbon disk electrode (GCDE) with a diameter of 5 mm was used as the support for the working electrode. The GCDE was polished with α-Al_2O_3 powder of decreasing sizes (1.0 μm to 50 nm) and was ultrasonically washed with deionized water and absolute ethanol. 5 mg catalysts were mixed with 30 μL Nafion solution; it was then dispersed in 1 mL of isopropanol solution and sonicated for 1 h to form a homogeneous ink. Subsequently, 5 μL of the dispersion solutions were dropped onto the GCDE surface using a micropipette and dried at ambient temperature. The reference electrode was an Ag|AgCl/KCl (saturated) electrode and the counter electrode was a Pt wire.

All the potentials were calibrated to the reversible hydrogen electrode (RHE), using the following equation: E(RHE)=E(Ag/AgCl)+(0.197+0.059×pH) V. The polarization curves were recorded using linear sweep voltammetry with a scan rate of 5 mV s^{-1} in 0.1 M KOH solutions after purging

with oxygen for 30 min. We applied an *iR* correction (resistive drop) to all the original data for further analysis. The electrical double layer capacitance (C_{dl}) of the as-synthesized materials was measured from double-layer charging curves using cyclic voltammograms (CVs) in a small potential range. The plot of the current density (at 1.14 V) against scan rate has a linear relationship and its slope is the double layer capacitance (C_{dl}) of the tested catalyst. AC impedance measurements of the catalysts were performed in the same configuration at various overpotentials with frequency from 100 kHz to 0.01 Hz and amplitude of 5 mV. The Nyquist plots were thus obtained based on the electrochemical impedance spectroscopy data. For the chronoamperometric test, a static overpotential was fixed for a certain time during continuous OER process to obtain the curve of time dependence of the current density.

Zn-air battery (ZAB) measurements

The Zn-air battery (ZAB) tests were performed with a homemade Zn-air cell. The air cathode was made by spraying a certain volume of catalyst ink onto a carbon paper with a gas diffusion layer with a catalyst loading of 0.25 mg cm^{-2}. The catalyst ink was prepared by ultrasonically dispersing a mixture of 6 mg Ni_2Mo_3N and 6 mg iron phthalocyanine (FePc), 12 mL ethanol and 100 μL of 5 wt% Nafion solution. For comparison, a mixture of 40 % Pt/C and RuO_2 (mass ratio 1:1) with the same loading was used as the catalytic layer. A polished zinc foil (thickness: 0.3 mm) was used as the anode and the electrolyte was 6.0 M KOH containing 0.20 M $Zn(Ac)_2$. A Land CT2001A system was used to carry out the cycling test with a ten-minute rest time between each discharge and charge at a current density of 10 mA cm^{-2}. Each discharge and charge period were set to be 30 min. The charge and discharge polarization curves were carried out using the PINE electrochemical workstation (Pine Research Instrumentation, USA).

Computational details

Density functional theory (DFT) calculations were performed using the Vienna *Abinitio* Simulation Package (VASP) version 5.4.4.[32, 33] and Quantum Espresso (QE) Package.[34] The projector augmented method (PAW) was used to treat the interactions between ions and core electrons.[35] The *1s* of H, *2s2p* of C, N and O, *3d4s* of Ni, and *4d5s* of Mo were treated as valence electrons. We used the Perdew-Burke-Ernzerhof (PBE) as exchange-correlation functional.[36] For Ni_2Mo_3N, standard DFT with PBE functional was employed. For NiO bulk and slab structure, we applied the DFT+U method.[37] The U_{eff} = U-J value of 5.5 eV was chosen, following from previous computational study on β-$Ni(OH)_2$ and β-NiOOH by J.Tkalych et al.[38] The energy cutoff for valence electronic structures was 600 eV for all structures. A Monkhorst-pack k-point mesh was used to sample the Brillouin zone with 3x3x3 for bulk Ni_2Mo_3N, 6x6x6 for bulk NiO, and 3x3x1 for slab models of hybrid NiO/Ni_2Mo_3N structure and pure NiO, respectively.

Spin polarized calculations with the antiferromagnetic configuration of Ni in NiO were performed. Structure models used in our calculations were presented in Supplementary Figs. 16 and 17. The (111) surface slab of Ni_2Mo_3N built was ~11 Å thick. An O-terminated five atomic layer of (3x3) NiO (111), with its O layer in contact with Ni_2Mn_3N (111), was added on top to construct the hybrid structure (denoted as "NiO/Ni_2Mo_3N"). The NiO overlayer is subjected to ~5% tensile strain in this hybrid structure. An O-terminated nine atomic layer of (3x3) NiO (111) slab models used to model pure NiO surface. The atoms within bottom 3 Å were fixed at their optimized bulk positions, in order to mimic the presence of bulk crystal underneath. Five out of nine O atoms on the O-terminated surface of NiO (111) was bonded with hydrogen to form OH species (Supplementary Fig.17). The reduced coverage was used to model deprotonation under basic condition[39] and the resulting structure shares a similar feature as the (001) β-NiOOH surface.[38] Two different positions, at a different distance to reactive sites, were investigated for Mo doping (Supplementary Fig.17). At least 12 Å of vacuum was used to prevent interactions between surfaces and periodic images in the slab calculations.

Previous studies of OER over Ni oxide surfaces suggest that the OER critically depends on the deprotonation of OH and formation of OOH species. We focus on study of the following two critical steps (* indicates a surface site):

$$*OH \rightarrow *O + H^+ + e^-(A)$$

$$H_2O + *O \rightarrow *OOH + H^+ + e^-(B)$$

Standard hydrogen electrode was used to reference the energy of H^+ and e^-. We calculated the formation free energy of *OH, *O and *OOH as follows:

$$\Delta G_{*\mathrm{O}} = E_{*\mathrm{O}} - E_{*} - E_{\mathrm{H_2O}} + E_{\mathrm{H_2}} + \Delta ZPE - T\Delta S - \Delta G_{\mathrm{H_2O}}^{Cond}$$

$$\Delta G_{*\mathrm{OH}} = E_{*\mathrm{OH}} - E_{*} - E_{\mathrm{H_2O}} + 0.5E_{\mathrm{H_2}} + \Delta ZPE - T\Delta S - \Delta G_{\mathrm{H_2O}}^{Cond}$$

$$\Delta G_{*\mathrm{OOH}} = E_{*\mathrm{OOH}} - E_{*} - 2E_{\mathrm{H_2O}} + 1.5E_{\mathrm{H_2}} + \Delta ZPE - T\Delta S - 2\Delta G_{\mathrm{H_2O}}^{Cond}$$

Here E_X indicates DFT total energies for X species. Zero-point energy corrections were calculated based on vibrational frequencies of the adsorbed species or isolated molecules. The entropy and free energy change of water from gas to liquid at 298 K (-0.089 eV) were taken from NIST WebBook. These correction terms are summarized in Table S4. Therefore, the reaction free energy can be calculated as

$$\Delta G_{\mathrm{A}} = \Delta G_{*\mathrm{O}} - \Delta G_{*\mathrm{OH}}$$

$$\Delta G_{\mathrm{B}} = \Delta G_{*\mathrm{OOH}} - \Delta G_{*\mathrm{O}}$$

The overpotential can be estimated as $max\ (\Delta G_{\mathrm{A}}, \Delta G_{\mathrm{B}})/e - 1.23$, where 1.23 V is the experimental thermodynamic potential for water splitting.

Acknowledgment

This work is supported by Natural Science Foundation of China (Grant No. 21471147) and National Key Research and Development Plan (Grant No. 2016YFB0101205). X.G. and Y.Z.

thank the Hong Kong Research Grants Council through the Early Career Scheme (project No. 25301617) for financial support. MY would like to thank the National “Thousand Youth Talents” program of China and Ningbo 3315 program for support. JPA thanks EPSRC for support. TT thanks DST of India for financial support for work on energy harnessing (via DSEHC) and energy storage and conversion (via MES). PL would like to acknowledge the Donors of the American Chemical Society Petroleum Research Fund for support of the computational research. X.G. and Y.Z. thank Dr. Wei Lu for optimizing the JEOL JEM-2100F microscope in the Hong Kong Polytechnic University.

Reference

[1] Fabbri E, Nachtegaal M, Binninger T, Cheng X, Kim BJ, Durst J, et al. Dynamic surface self-reconstruction is the key of highly active perovskite nano-electrocatalysts for water splitting. Nature Materials. 2017;16.

[2] Roy C, Sebok B, Scott S, Fiordaliso E, Sørensen J, Bodin A, et al. Impact of nanoparticle size and lattice oxygen on water oxidation on NiFeO x H y. Nature Catalysis. 2018;1:820.

[3] Yan J, Kong L, Ji Y, White J, Li Y, Zhang J, et al. Single atom tungsten doped ultrathin α-Ni (OH) 2 for enhanced electrocatalytic water oxidation. Nature communications. 2019;10:2149.

[4] Bak J, Bae HB, Chung S-Y. Atomic-scale perturbation of oxygen octahedra via surface ion exchange in perovskite nickelates boosts water oxidation. Nature Communications. 2019;10:2713.

[5] Retuerto M, Pascual L, Calle-Vallejo F, Ferrer P, Gianolio D, Pereira AG, et al. Na-doped ruthenium perovskite electrocatalysts with improved oxygen evolution activity and durability in acidic media. Nature communications. 2019;10:2041.

[6] Yu F, Zhou H, Zhu Z, Sun J, He R, Bao J, et al. Three-dimensional nanoporous iron nitride film as an efficient electrocatalyst for water oxidation. ACS Catalysis. 2017;7:2052-7.

[7] Zhang Y, Ouyang B, Xu J, Jia G, Chen S, Rawat RS, et al. Rapid synthesis of cobalt nitride nanowires: Highly efficient and low‐cost catalysts for oxygen evolution. Angewandte Chemie International Edition. 2016;55:8670-4.

[8] Xu K, Chen P, Li X, Tong Y, Ding H, Wu X, et al. Metallic nickel nitride nanosheets realizing enhanced electrochemical water oxidation. Journal of the American Chemical Society. 2015;137:4119-25.

[9] Defilippi C, Shinde DV, Dang Z, Manna L, Hardacre C, Greer AJ, et al. HfN Nanoparticles: An Unexplored Catalyst for the Electrocatalytic Oxygen Evolution Reaction. Angewandte Chemie International Edition. 2019;58:15464-70.

[10] Zhao S, Li M, Han M, Xu D, Yang J, Lin Y, et al. Defect‐Rich Ni3FeN Nanocrystals Anchored on N‐Doped Graphene for Enhanced Electrocatalytic Oxygen Evolution. Advanced Functional Materials. 2018;28:1706018.

[11] Wang Y, Liu D, Liu Z, Xie C, Huo J, Wang S. Porous cobalt–iron nitride nanowires as excellent bifunctional electrocatalysts for overall water splitting. Chemical Communications. 2016;52:12614-7.

[12] Cao B, Veith GM, Diaz RE, Liu J, Stach EA, Adzic RR, et al. Cobalt molybdenum oxynitrides: synthesis, structural characterization, and catalytic activity for the oxygen reduction reaction. Angewandte Chemie International Edition. 2013;52:10753-7.
[13] Fei H, Dong J, Feng Y, Allen CS, Wan C, Volosskiy B, et al. General synthesis and definitive structural identification of MN 4 C 4 single-atom catalysts with tunable electrocatalytic activities. Nature Catalysis. 2018;1:63-72.
[14] Yan Y, Xia BY, Zhao B, Wang X. A review on noble-metal-free bifunctional heterogeneous catalysts for overall electrochemical water splitting. Journal of Materials Chemistry A. 2016;4:17587-603.
[15] Zheng Y, Jiao Y, Jaroniec M, Qiao SZ. Advancing the Electrochemistry of the Hydrogen‐Evolution Reaction through Combining Experiment and Theory. Angewandte Chemie International Edition. 2015;54:52-65.
[16] Xue Z, Li X, Liu Q, Cai M, Liu K, Liu M, et al. Interfacial electronic structure modulation of NiTe nanoarrays with NiS nanodots facilitates electrocatalytic oxygen evolution. Advanced Materials. 2019;31:1900430.
[17] Wang B, Tang C, Wang HF, Chen X, Cao R, Zhang Q. A Nanosized CoNi Hydroxide@ Hydroxysulfide Core–Shell Heterostructure for Enhanced Oxygen Evolution. Advanced Materials. 2019;31:1805658.
[18] Roy C, Sebok B, Scott S, Fiordaliso E, Sørensen J, Bodin A, et al. Impact of nanoparticle size and lattice oxygen on water oxidation on NiFeO x H y. Nature Catalysis. 2018;1:820-9.
[19] Nong HN, Reier T, Oh H-S, Gliech M, Paciok P, Vu THT, et al. A unique oxygen ligand environment facilitates water oxidation in hole-doped IrNiO x core–shell electrocatalysts. Nature Catalysis. 2018;1:841-51.
[20] Valerio M, Cristina G, Markus A, Davide E. Titanium nitride-nickel nanocomposite as heterogeneous catalyst for the hydrogenolysis of aryl ethers. Journal of the American Chemical Society. 2014;136:1758-61.
[21] Yu Q, Lian G. Metal‐Urea Complex—A Precursor to Metal Nitrides. Journal of the American Ceramic Society. 2010;87:352-7.
[22] Giordano C, Erpen C, Yao W, Antonietti M. Synthesis of Mo and W carbide and nitride nanoparticles via a simple "urea glass" route. Nano Letters. 2008;8:4659-63.
[23] Errandonea D, Ferrer-Roca C, Martínez-Garcia D, Segura A, Gomis O, Muñoz A, et al. High-pressure x-ray diffraction and ab initio study of Ni 2 Mo 3 N , Pd 2 Mo 3 N , Pt 2 Mo 3 N , Co 3 Mo 3 N , and Fe 3 Mo 3 N : Two families of ultra-incompressible bimetallic interstitial nitrides. Physrevb. 2010;82:1616-22.
[24] Herle PS, Hegde MS, Sooryanarayana K, Row TNG, Subbanna GN. ChemInform Abstract: Ni 2 Mo 3 N: A New Ternary Interstitial Nitride with a Filled β-Manganese Structure. Inorganic Chemistry. 1998;29:4128.
[25] Alconchel S, Sapiña F, Beltrán D, Beltrán A. Chemistry of interstitial molybdenum ternary nitrides MnMo3N (M=Fe, Co, n=3; M=Ni, n=2). Journal of Materials Chemistry. 1998;8:1901-9.
[26] Alconchel S, Sapin F, Beltran D, Beltran A. A new approach to the synthesis of molybdenum bimetallic nitrides and oxynitrides. J Mater Chem. 1999;9:749-55.
[27] Tian X, Luo J, Nan H, Zou H, Chen R, Shu T, et al. Transition metal nitride coated with atomic layers of Pt as a low-cost, highly stable electrocatalyst for the oxygen reduction reaction. Journal of the American Chemical Society. 2016;138:1575-83.

[28] Jain A, Shin Y, Persson KA. Computational predictions of energy materials using density functional theory. Nature Reviews Materials. 2016;1:1-13.
[29] Nørskov JK, Abild-Pedersen F, Studt F, Bligaard T. Density functional theory in surface chemistry and catalysis. Proceedings of the National Academy of Sciences. 2011;108:937-43.
[30] Tkalych AJ, Zhuang HL, Carter EA. A density functional+ U assessment of oxygen evolution reaction mechanisms on β-NiOOH. ACS Catalysis. 2017;7:5329-39.
[31] Tkalych AJ, Martirez JMP, Carter EA. Effect of transition-metal-ion dopants on the oxygen evolution reaction on NiOOH (0001). Physical Chemistry Chemical Physics. 2018;20:19525-31.
[32] Kresse G. Ab initio molecular dynamics for liquid metals. Phys Rev B Condens Matter. 1993;48:13115-8.
[33] Kresse G, Furthmüller J. Efficiency of ab-initio total energy calculations for metals and semiconductors using a plane-wave basis set. Computational materials science. 1996;6:15-50.
[34] Giannozzi P, Baroni S, Bonini N, Calandra M, Car R, Cavazzoni C, et al. QUANTUM ESPRESSO: a modular and open-source software project for quantum simulations of materials. Journal of physics: Condensed matter. 2009;21:395502.
[35] PE B. Projector augmented-wave method. Phys Rev B Condens Matter. 1994;50:17953-79.
[36] Perdew JP, Burke K, Ernzerhof M. Generalized Gradient Approximation Made Simple. Physical Review Letters. 1998;77:3865-8.
[37] Dudarev SL, Botton GA, Savrasov SY, Humphreys CJ, Sutton AP. Electron-energy-loss spectra and the structural stability of nickel oxide: An LSDA+U study. Physical Review B. 1998;57:1505-9.
[38] Tkalych AJ, Kuang Y, Carter EA. Structural and Electronic Features of β-Ni(OH)2 and β-NiOOH from First Principles. Journal of Physical Chemistry C. 2015;119:24315-22.
[39] Zaffran J, Toroker MC. A deep understanding of oxygen evolution reaction on two‐dimensional NiO2 catalyst. Chemelectrochem. 2017.